EUROfusion

EUROFUSION WP15ER–PR(15)22

J.A. Morales et al.

Edge Localized Mode Rotation and the Nonlinear Dynamics of Filaments

Preprint of Paper to be submitted for publication in
Physical Review Letters

This work has been carried out within the framework of the EUROfusion Consortium and has received funding from the Euratom research and training programme 2014-2018 under grant agreement No 633053. The views and opinions expressed herein do not necessarily reflect those of the European Commission.

"This document is intended for publication in the open literature. It is made available on the clear understanding that it may not be further circulated and extracts or references may not be published prior to publication of the original when applicable, or without the consent of the Publications Officer, EUROfusion Programme Management Unit, Culham Science Centre, Abingdon, Oxon, OX14 3DB, UK or e-mail Publications.Officer@euro-fusion.org".

"Enquiries about Copyright and reproduction should be addressed to the Publications Officer, EUROfusion Programme Management Unit, Culham Science Centre, Abingdon, Oxon, OX14 3DB, UK or e-mail Publications.Officer@euro-fusion.org".

The contents of this preprint and all other EUROfusion Preprints, Reports and Conference Papers are available to view online free at http://www.euro-fusionscipub.org. This site has full search facilities and e-mail alert options. In the JET specific papers the diagrams contained within the PDFs on this site are hyperlinked.

Edge Localized Mode Rotation and the Nonlinear Dynamics of Filaments

J.A. Morales,* M. Bécoulet, X. Garbet, G. Dif-Pradalier,
A. Fil, E. Nardon, C. Passeron, and G. Latu
CEA, IRFM, 13108 Saint-Paul-Lez-Durance, France

F. Orain and M. Hoelzl
Max Planck Institute for Plasma Physics,
Boltzmannstr. 2, 85748 Garching, Germany

S. Pamela
EUROfusion Consortium, JET, Culham Science Centre,
Abingdon OX14 3DB, United Kingdom

P. Cahyna
Institute of Plasma Physics ASCR, 182 00 Prague 8, Czech Republic

G.T.A. Huijsmans
ITER Organization, Route de Vinon sur Verdon,
13115 Saint Paul Lez Durance, France

(Dated: July 13, 2015)

Abstract

The existence of Edge Localised Modes (ELM) rotating precursors few milliseconds before an ELM crash was reported in many experiments (KSTAR, MAST, AUG, NSTX, TCV, JET). Moreover, in these experiments, similar nonlinear dynamics are observed at the ELM crash. In the present letter, the rotation of ELM precursors and the dynamics of expelled filaments at the ELM crash are explained using both, linear ballooning theory and nonlinear MHD simulations with the JOREK code. It is shown that unstable ballooning modes, localised at the pedestal, grow and rotate mainly in the electron diamagnetic direction in the laboratory reference frame. Approaching the ELM crash, this regular rotation decreases corresponding to the moment when the magnetic reconnections and edge ergodisation occur. During the highly nonlinear ELM crash, the ELM filaments are cut from the main plasma due to the strong sheared mean flow that is nonlinearly generated via the Maxwell stress tensor.

* Email: jorge.a.morales@outlook.com

I. INTRODUCTION

Edge Localised Modes are MHD instabilities that appear at the edge of the tokamak plasma in high confinement mode (H-mode). They are characterised by periodic bursts of matter and energy. The crash of this instability leads to the relaxation of the edge pressure pedestal. Then the edge pedestal rebuilds and another ELM cycle occurs. The quantity of energy that is expelled periodically can cause partial erosion or melting of plasma-facing components (PFC). This could limit the operational capabilities of future larger tokamak devices like ITER and DEMO. For recent review articles on ELMs we refer to [1, 2].

In recent years, measurements performed with electron cyclotron emission imaging (ECEI) have provided insights on the dynamics of this instability prior to and during an ELM crash. ECEI measurements in the KSTAR tokamak [3] show that the ELM evolution can be separated in three different phases. The first is a linear phase where the localised mode grows, the second is a quasi-quiescent state where the mode growth decreases and the third is when the ELM crash occurs. In the majority of cases, during the linear phase, the rotation of the precursors (structures preceding an ELM crash) is observed in the electron diamagnetic direction. Near the crash, the rotation speed of the precursors decreases and the precursor structure seems to extend radially towards the last closed flux surface where the ELM crash occurs. These measurements are in agreement with AUG ECEI measurements [4, 5]. In AUG, the rotation of the ELM precursors is also found in the electron diamagnetic direction but the first-expelled ELM filament is observed to reverse rotation and to propagate in the ion diamagnetic direction. In a third device, NSTX, gas puffing imaging is used to characterise the precursors rotation and the filament expulsion of an ELM [6]. In this last device the precursors are also observed rotating in the electron diamagnetic direction and at the crash, the filament slow down and also reverses rotation direction (propagating in the ion diamagnetic direction). In TCV with magnetic measurements [7] and in MAST using beam emission spectroscopy [8] similar results were obtained. Recently in JET, fast infra-red thermography measurements at the divertor [9] show ELM precursors stripes moving radially outward. This also suggests ELM precursors structures rotating in the electron diamagnetic direction.

Several instabilities can be candidate to explain the ELM precursors. The microtearing mode instability has been proposed as one of the possible candidates [8, 10]. This instability

shares several characteristics with the experimental measurements but its radial extend is short (of the order of the ion Larmor radius). This last feature is incompatible with some of the observations. Also peeling modes and drift waves can be considered but, the firsts are characterised by low toroidal mode numbers that are inconsistent with the observations and the seconds are electrostatic in nature, a characteristic not compatible with the electromagnetic properties of ELM precursors.

Ballooning modes are strong candidates to explain the observations [11]. In this manuscript we will focus on this last instability. Analytically in the linear phase we consider ideal and resistive ballooning modes taking into account bi-fluid diamagnetic effects. Numerical calculations using the nonlinear code JOREK [12, 13] are performed. A comparison with the analytical results in the linear stage is carried out. This numerical code is also used to analyse the nonlinear saturation of the instability and to characterise the mechanism that allows to explain the reversal of the filaments rotation at the ELM crash.

II. THE LINEAR BALLOONING MODE ROTATION

The reduced MHD equations over the magnetic flux Ψ, the electric potential Φ and the pressure P, are used to calculate the dispersion relation associated with the ballooning instability. We use the gyro-viscous cancellation to simplify the equation over Φ (see e.g. [14]). The ballooning representation is used to reduce the two-dimensional problem to one dimension (see e.g. [15]). The following ansatz is applied

$$\Phi(\phi,\theta,t) = \sum_{l=-\infty}^{+\infty} \widehat{\Phi}(\theta+2\pi l) e^{i(n[\phi - q(\theta+2\pi l)] - \omega t)}, \tag{1}$$

for a ballooning mode $l = 0$. Also, for simplification, we consider the reference frame rotating with the $\boldsymbol{E}\times\boldsymbol{B}$ velocity, hence in this reference frame $V_{\boldsymbol{E}\times\boldsymbol{B}} = 0$ ($\widehat{\Phi}_{n=0} = 0$). We will add the $\boldsymbol{E}\times\boldsymbol{B}$ velocity contribution at the end of the linear calculation.

Using these hypothesis the following dispersion relation, in dimensionless form, is found

$$\omega(\omega-\omega_i^*)\left[(\omega-\omega_e^*) + \frac{q^2R_0^2\left(\omega-\omega_e^*+i\eta k_\theta^2\right)^2}{i\eta k_\theta^2 s^2}\left[\omega\left(\omega-\omega_i^*\right)+2\gamma_I^2\right]\right] \quad + \\ \gamma_I^2\left(\omega-\omega_e^*\right)\left(1+\frac{\left(\omega-\omega_e^*+i\eta k_\theta^2\right)\left(2s\left(1-s\right)-1\right)}{2i\eta k_\theta^2 s^2}\right) = \frac{-q^2R_0^2\left(\omega-\omega_e^*+i\eta k_\theta^2\right)^2}{i\eta k_\theta^2 s^2}\gamma_I^4, \tag{2}$$

with $\omega_i^* = -\omega_e^* = d_i \frac{\partial P_0}{\partial r} k_\theta \, \boldsymbol{e}_\theta$, $d_i = \frac{1}{\omega_{Ci}\tau_A} = \frac{m_i}{eR_0\sqrt{\rho_0\mu_0}}$ and $\gamma_I = \left\{ -\frac{4}{B_0 R_0}\frac{\partial P_0}{\partial r} \right\}^{1/2}$, with θ the poloidal direction, k_θ the poloidal wavenumber, $\omega^*_{i/e}$ the diamagnetic frequencies (ion/electron, non-dimensionalised by the Alfvén time τ_A), d_i the diamagnetic parameter, γ_I the ideal interchange growth rate, P_0 the axisymmetric pressure, q the safety factor, s the magnetic shear and η the dimensionless inverse Lundquist number. Also B_0, ρ_0, R_0, μ_0 and e are respectively a reference magnetic field, density, length, the magnetic permeability and electric charge.

At high resistivity ($\eta \to \infty$) and strong magnetic shear ($s >> 1$) Eq. (2) simplifies to

$$\omega(\omega - \omega_i^*)(\omega - \omega_e^*) = (i\gamma_\eta)^3 \;\text{ with }\; \gamma_\eta = \left[\frac{k_\theta^2 q^2}{s^2} R_0^2 \eta \gamma_I^4 \right]^{1/3}. \tag{3}$$

Considering the diamagnetic frequencies: $\omega_i^* = -\omega_e^* = \omega_*$, the roots of the polynomial can be found using Cardan's method. Taking into account the change of variable: $\omega = i\gamma$, this dispersion relation can be simplified to

$$\gamma\left(\gamma^2 + \omega_*^2\right) = \gamma_\eta^3. \tag{4}$$

Two limits can be identified in Eq. (4), for $\gamma_\eta >> \omega_*$ the solution $\gamma \approx \gamma_\eta$ and if $\gamma_\eta << \omega_*$ we have $\gamma \approx \gamma_\eta^3/\omega_*^2$. In the general case three roots exist, one real and two complex conjugates [16]. The most unstable root is always the real, the value of ω is pure imaginary because $\omega = i\gamma$, hence at this limit the unstable mode does not rotate in the considered reference frame.

Also at the ideal limit, $\eta \to 0$, and small magnetic shear ($s \approx 1$) the dispersion relation Eq. (2) simplifies to the second order polynomial [17, 18]

$$\omega^2 - \omega_i^* \omega + \gamma_I^2 = 0. \tag{5}$$

Two distinct roots exist

$$\omega_\pm = \frac{\omega_i^* \pm \sqrt{\omega_i^{*2} - 4\gamma_I^2}}{2}. \tag{6}$$

The system is unstable if: $|\omega_i^*/2| < |\gamma_I|$. And the ideal rotation frequency of the mode is: $\omega_i^*/2$ [19, 20]. In this case the unstable mode rotates at half of the diamagnetic frequency in the ion diamagnetic direction in the considered reference frame.

Moreover the roots of the general dispersion relation, Eq. (2), can be computed numerically. We find that in realistic cases, i.e., at low resistivity ($\eta < 10^{-7}$) the most unstable

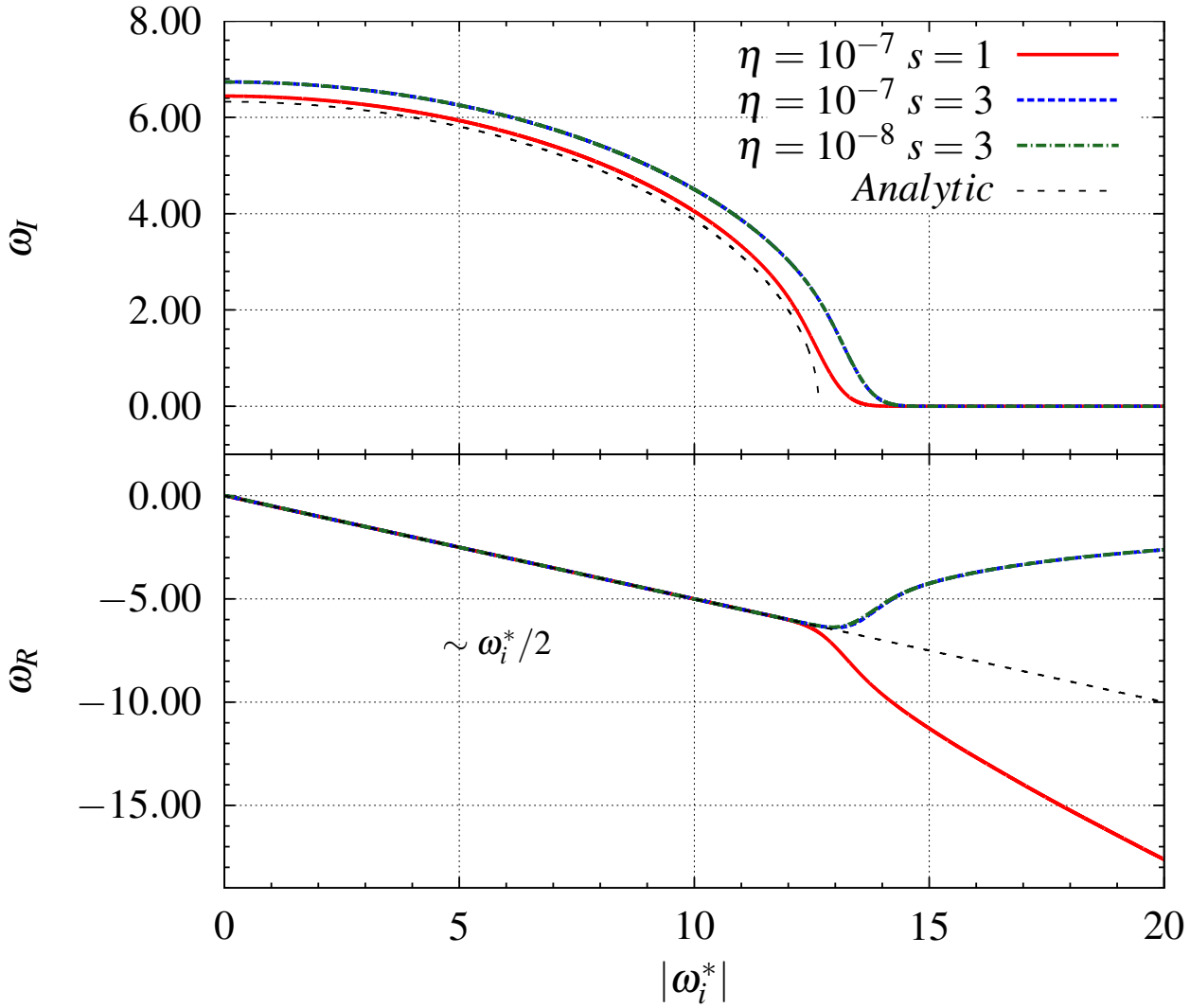


FIG. 1. Evolution of the roots with the diamagnetic frequency ω_i^*, (top) imaginary part (bottom) real part.

root is close to the ideal case Eq. (6). In Fig. 1 three computed cases are compared to the analytical solution Eq. (6). One can observe that the imaginary part of the root is close to the ideal theory if the magnetic shear is small. With increasing magnetic shear the calculated mode is more unstable. On the other hand the real part of the root matches very well the analytical solution. The rotation of the mode, in the reference frame, is almost exactly $\omega_i^*/2$.

To calculate the mode poloidal rotation, in the laboratory reference frame, we add to the intrinsic ballooning mode rotation the poloidal $\boldsymbol{E} \times \boldsymbol{B}$ velocity and the parallel velocity $V_{/\!/} \cdot b_\theta$ (both velocities projected in the poloidal plane). The radial electric field in H-mode

is observed to be dominated at the pedestal by the radial pressure gradient of the main ions [21]. Also the pitch angle is considered to be small ($\boldsymbol{B}$ is mainly in the toroidal direction). For these two reasons, in the pedestal region, the poloidal $\boldsymbol{E}\times\boldsymbol{B}$ velocity $V_{\boldsymbol{E}\times\boldsymbol{B}}$ can be approximated by

$$V_{\boldsymbol{E}\times\boldsymbol{B}} \approx (\boldsymbol{E}\times\boldsymbol{B})/B^2 \approx (\nabla_r P_i \times \boldsymbol{B}) / \left(enB^2\right). \tag{7}$$

Finally the poloidal rotation of the ballooning modes in the laboratory reference frame for the resistive and ideal limits writes

$$\text{Resistive:}\quad V_{\text{mode}} = V_{\boldsymbol{E}\times\boldsymbol{B}} + V_{/\!/}\cdot b_\theta \tag{8}$$

$$\text{Ideal:}\quad V_{\text{mode}} = V_{\boldsymbol{E}\times\boldsymbol{B}} + V_{/\!/}\cdot b_\theta + V_i^*/2, \tag{9}$$

with the poloidal ion diamagnetic velocity $V_i^* \approx (\boldsymbol{B}\times\nabla P_i)/(enB^2)$. In dimensionless units (non-dimensionalised by the Alfvén speed) this velocity becomes

$$V_i^* = \omega_i^*/k_\theta \approx d_i \nabla_r P. \tag{10}$$

Also the poloidal dimensionless $\boldsymbol{E}\times\boldsymbol{B}$ velocity at the pedestal, where the radial electric field is mostly induced by the radial pressure gradient, can be approximated by

$$V_{\boldsymbol{E}\times\boldsymbol{B}} \approx -d_i \nabla_r P. \tag{11}$$

The radial gradient of the pressure is negative. Therefore, by convention, we have chosen the $\boldsymbol{E}\times\boldsymbol{B}$ and electron diamagnetic velocities in the positive direction and the ion diamagnetic velocity in the negative direction.

Using the JOREK code [12, 22, 23] the linear growth of the ballooning instability with and without diamagnetic effects can be analysed. ELM precursors were previously observed with the JOREK code without diamagnetic effects [22]. Here we include diamagnetic effects to analyse their effect on the precursors dynamics. The parameters used for the simulations are close to a JET tokamak plasma, as in Ref. [24]. Realistic values of the inverse Lundquist number, d_i parameter and normalised parallel heat conductivity are typically: $\eta = 10^{-8}$, $d_i = 10^{-2}$ and $\kappa_{/\!/} = 8000$ [25]. These values correspond to the following tokamak parameters in JET: $R_0 = 2.9\,m$, $B_0 = 1.8\,T$, $n_{ped} = 3.3\cdot 10^{19}\,m^{-3}$ and $T_{e_{ped}} = T_{i_{ped}} = 1.8\,keV$.

The magnetic flux perturbation is presented in Fig. 2. Without diamagnetic effects, $d_i = 0$, the mode grows and rotates at low speed, as was found in Ref. [12]. On the

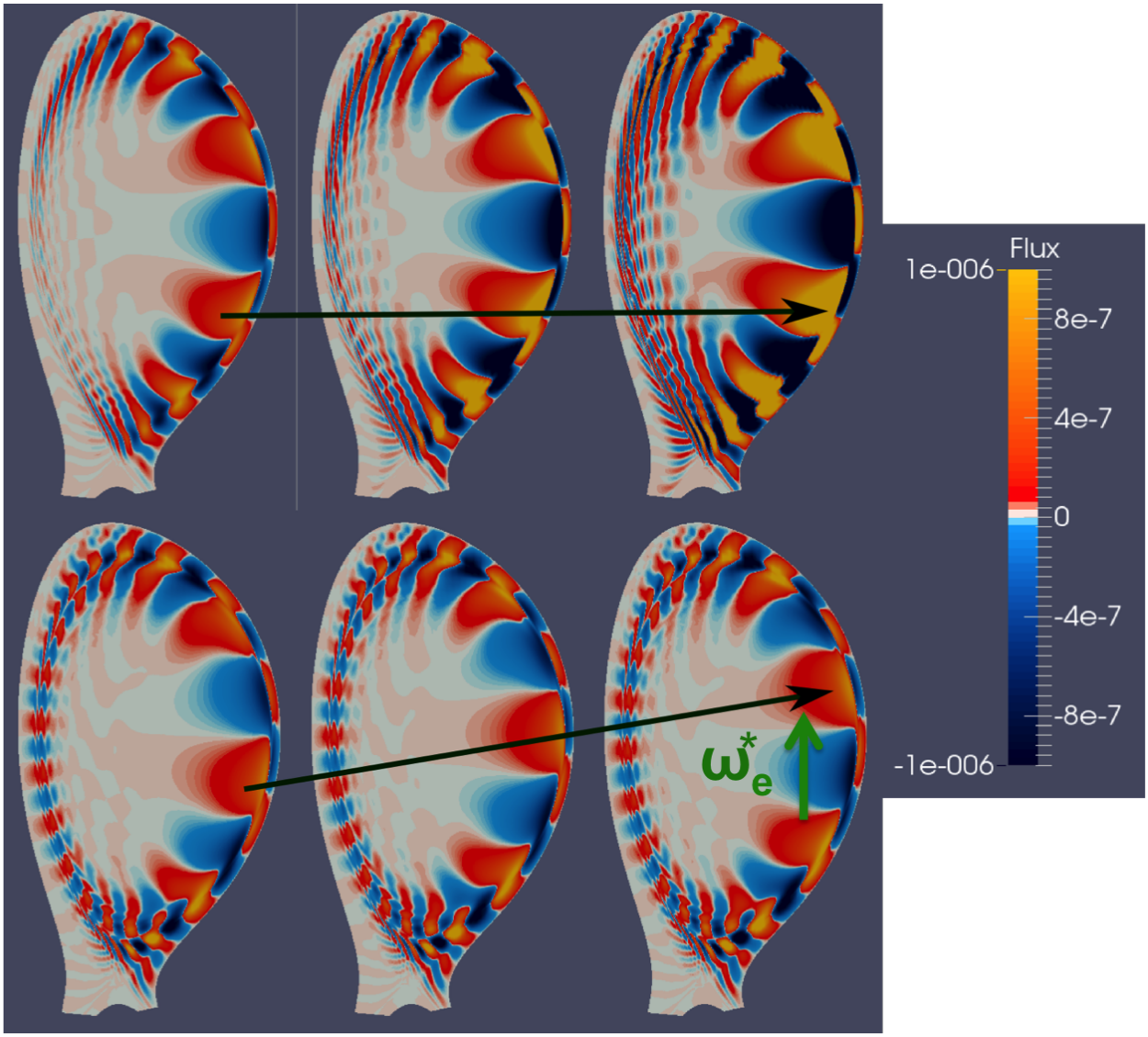


FIG. 2. Magnetic flux perturbation $n = 6$, same parameters as in Ref. [24] (10 μs between images), (top) without diamagnetic effects and (bottom) with diamagnetic effects, $d_i = 1.7 \cdot 10^{-2}$. In the bottom the rotation is anticlockwise, i.e., in the electron diamagnetic or $\boldsymbol{E} \times \boldsymbol{B}$ direction.

other hand, if diamagnetic effects are taken into account the mode rotates in the electron diamagnetic direction with a velocity of several km/s. The $\boldsymbol{E} \times \boldsymbol{B}$ velocity is strongly reduced if diamagnetic effects are not taken into account since this velocity is proportional to d_i at the pedestal (see Eq. (11)).

We perform several computations varying the diamagnetic parameter, the resistivity and the parallel heat conductivity. The ballooning mode velocity rotation is plotted against the diamagnetic parameter in Fig. 3. In this figure we observe a linear scaling with the

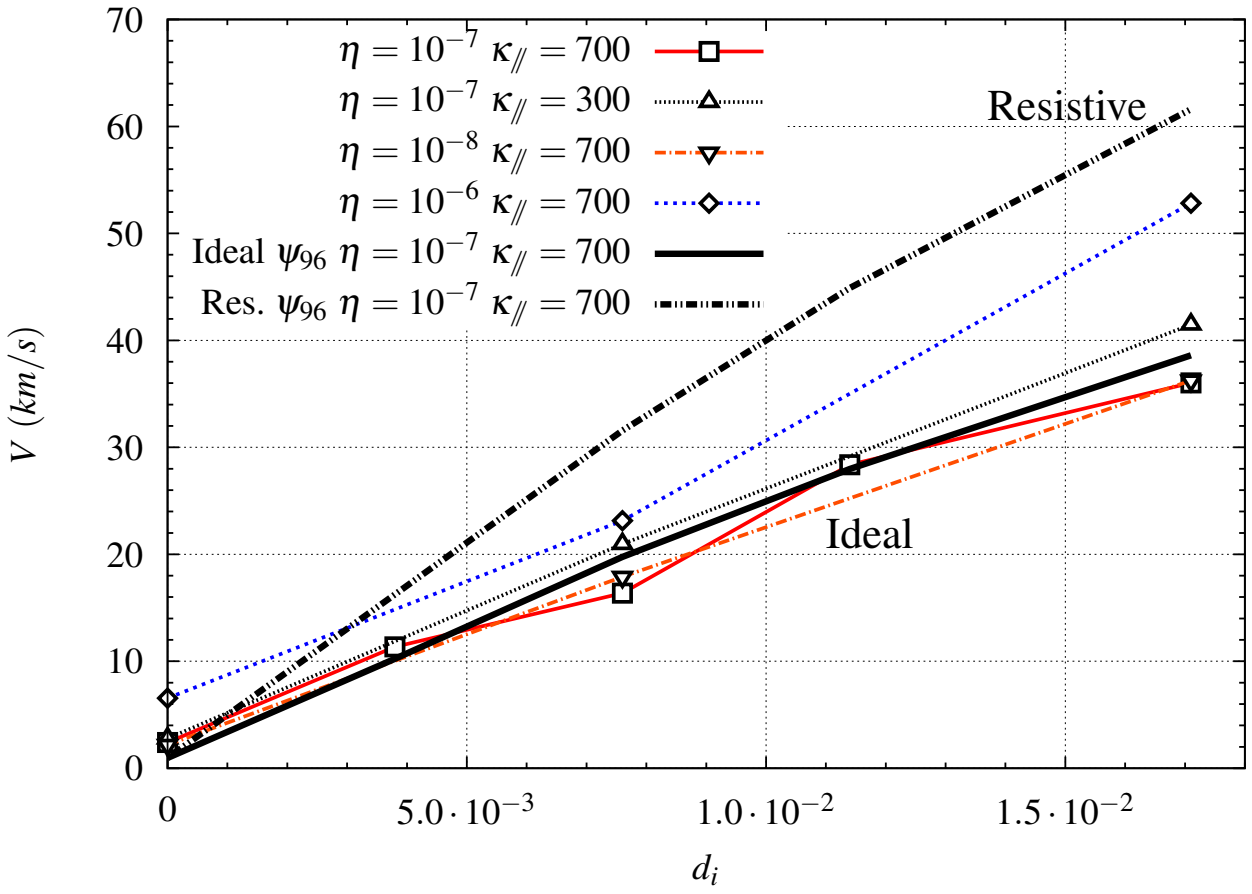


FIG. 3. Rotation velocity of the modes as a function of d_i and comparison with the expressions Eqs. (8) and (9) taked at Ψ_{96} (i.e. at the flux surface with $|\nabla P|_{max}$), $\kappa_{//}$ is the normalised parallel conductivity.

diamagnetic parameter d_i, in agreement with Eqs. (8) to (11).

In our simulations the $\boldsymbol{E} \times \boldsymbol{B}$ and the diamagnetic velocities dominate over the poloidally projected parallel velocity ($V_{//} \cdot b_\theta$). For small resistivities, the numerical computations are close to the ideal formula Eq. (9) (thick black curve in Fig. 3). We observe that the ballooning mode velocity is always dominated by the $\boldsymbol{E} \times \boldsymbol{B}$ velocity, this mode always rotates in the electron diamagnetic direction. This can be explained as follows: at the pedestal, the ion diamagnetic and $\boldsymbol{E} \times \boldsymbol{B}$ velocities have approximatively the same amplitude but opposite direction (see Eqs. (10) and (11)). For realistic cases (low resistivity) the system behaves close to the ideal limit. At this limit the ballooning mode rotates with half of the ion diamagnetic velocity (see Eq. (9)). As a consequence the $\boldsymbol{E} \times \boldsymbol{B}$ velocity is always larger and the ballooning mode rotates in the electron diamagnetic direction in the laboratory

reference frame.

In the present calculations we have not imposed a source of toroidal rotation. The parallel velocity comes from the Bohm boundary conditions that are imposed at the divertor. Therefore the projected parallel velocity is small compared to the $\boldsymbol{E} \times \boldsymbol{B}$ and diamagnetic velocities. In several devices as KSTAR the toroidal velocity can be very large. This velocity must be taken into account in the calculation of the ELM precursors rotation in the laboratory reference frame. Precursors rotating in the ion diamagnetic direction have also been observed. This behaviour can be explained by a strong toroidal rotation that counterbalances the $\boldsymbol{E} \times \boldsymbol{B}$ velocity.

III. NONLINEAR DYNAMICS OF ELM FILAMENTS

Experimentally the rotation of the modes is observed to decrease just before the ELM crash [3, 6]. Also the observations show the rotation of the ELM filaments in the ion diamagnetic direction [4, 6, 8]. This rotation is opposite to the one observed for the ELM precursors.

With the JOREK code the nonlinear evolution of the ballooning modes is studied for a case with $d_i = 7.6 \cdot 10^{-3}$. Near the ELM crash the density field can be observed on Fig. 4. In this image, filaments of high density are expelled in the ion diamagnetic direction as observed in the experiments.

The inversion of the rotation occurs at the nonlinear saturation of the instability. The perturbed electric potential grows creating periodic vortices with alternating positive and negative rotations. The strong correlation between the density and the electric potential can be observed on Fig. 5(a). The $V_{\boldsymbol{E}\times\boldsymbol{B}}$ vortices are deformed, they are thinner in the radial direction and elongated in the poloidal direction, following the magnetic field lines [26]. As observed in Fig. 5(a) the density filament is convected by the $\boldsymbol{E} \times \boldsymbol{B}$ velocity vortex. Also from the density ρ equation we can show that the density dynamic is governed by the $\boldsymbol{E} \times \boldsymbol{B}$ velocity term,

$$\frac{\partial \rho}{\partial t} = \frac{1}{R}\left[\rho R^2, \Phi\right] + d_i \, \frac{\partial P}{\partial Z} + \text{ Diff. } + \text{ Source}, \tag{12}$$

with the Poisson bracket defined as: $[f, g] = \boldsymbol{e}_\phi \cdot (\nabla f \times \nabla g)$ (cylindrical coordinates). In this equation the diamagnetic velocity (second term on the right hand side) does not act as an advection term but only as a compression term. Therefore only the $\boldsymbol{E} \times \boldsymbol{B}$ velocity convects

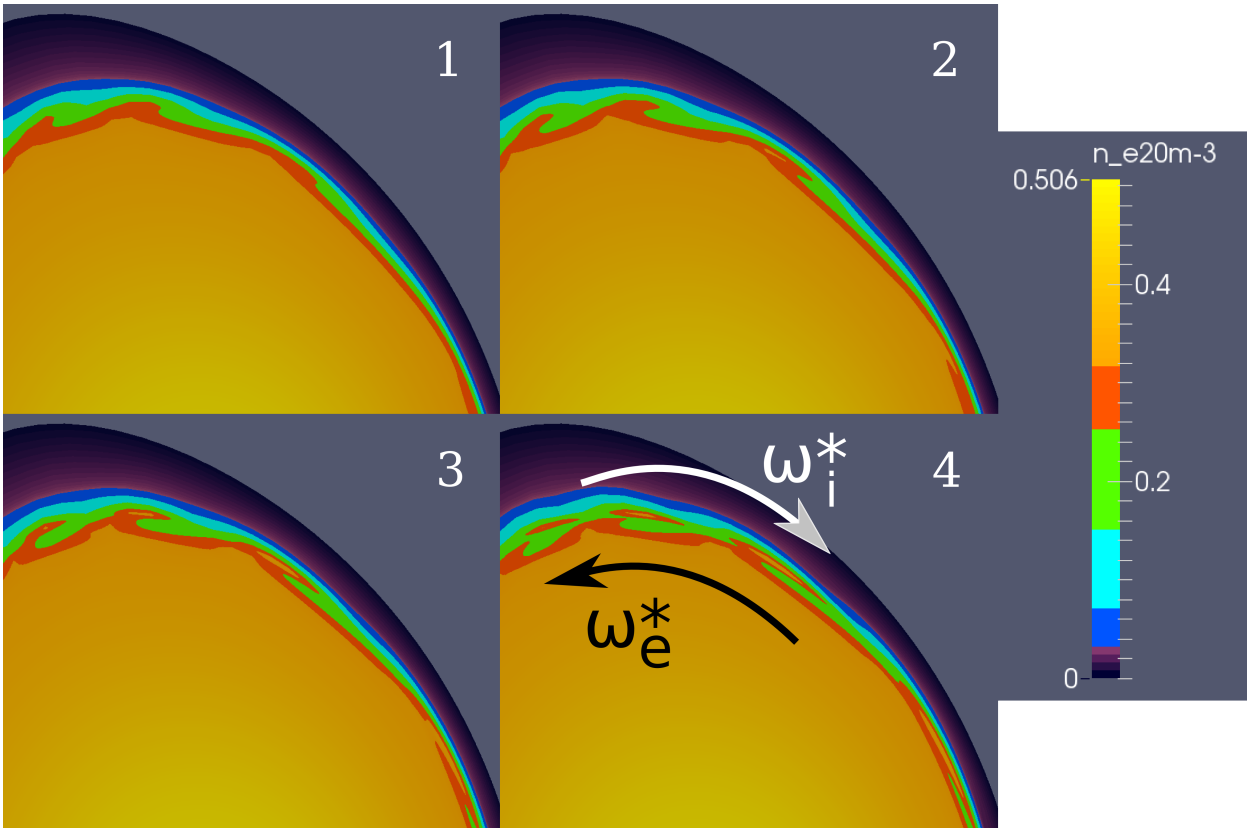
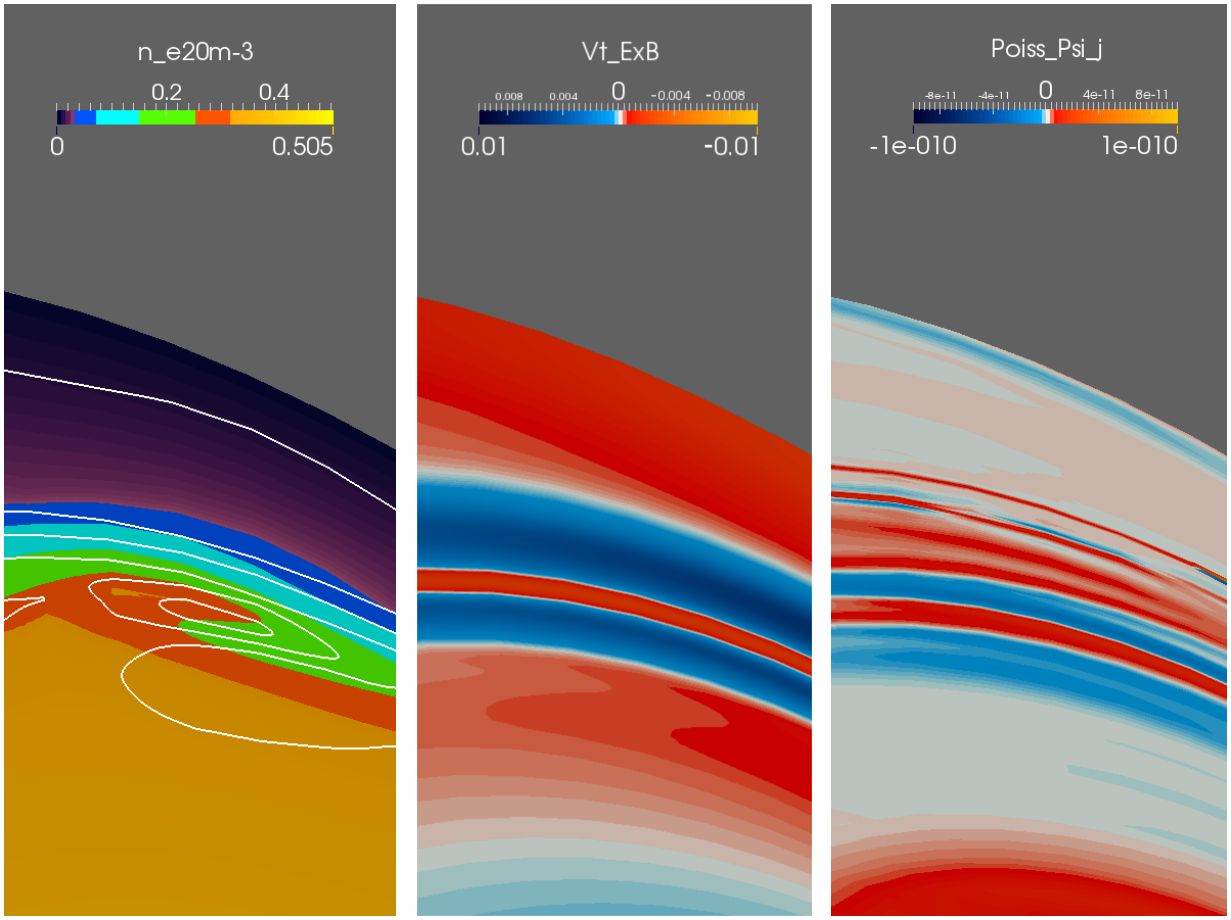


FIG. 4. Density filaments are expelled in ion diamagnetic direction, $d_i = 7.6 \cdot 10^{-3}$ (5 μs between images).

the density filament (first term on the right hand side). The diamagnetic velocity does not convect directly the density but plays an important role in the nonlinear interactions. As we show later, the diamagnetic effects have a non-negligible influence on the $\boldsymbol{E} \times \boldsymbol{B}$ vorticity.

The profiles of the axisymmetric component of the $\boldsymbol{E} \times \boldsymbol{B}$ velocity are plotted on Fig. 6 as a function of the normalised magnetic flux. From this figure we notice a strong velocity shear created during the ELM crash (see also Fig. 5(b)). At the same time as the filament is convected, a strong $\boldsymbol{E} \times \boldsymbol{B}$ shear appears. In the region where the mode perturbation is larger (around $\Psi_N = 0.96$) the velocity profile decreases and crosses the zero abscissa axis. This can explain why experimentally the ELM precursors decelerate approaching the crash. The shear increases further and the $\boldsymbol{E} \times \boldsymbol{B}$ velocity becomes negative. This effect makes the high density filament to cut from the main plasma, the filament is expelled.

Also in Ref. [12], without diamagnetic effects, a strong $\boldsymbol{E} \times \boldsymbol{B}$ shear was present in the nonlinear phase. The major difference with respect to the present computations is the initial



(a) (b) (c)

FIG. 5. (a) Density filament (colormap) and electric potential isocontours (white lines), (b) normalised axisymmetric $\boldsymbol{E}\times\boldsymbol{B}$ velocity and (c) Maxwell stress term $R^{-1}\left[\Psi, j\right]$. All these quantities are taken at the same instant, during the ELM crash ($t = 1273\ \mu s$ in Figs. 6 and 7).

$V_{\boldsymbol{E}\times\boldsymbol{B}}$ profile, the profile was close to zero in the cited reference.

The different terms of the $\boldsymbol{E}\times\boldsymbol{B}$ vorticity w_E equation, implemented in the JOREK code, are plotted as a function of time in Fig. 7 (averaged on the closed flux surface region for $n = 0$). In weak form the vorticity equation yields

$$\delta_t w_E = -\int \hat{\rho}\nabla u^* \cdot \nabla_\perp \left(\delta_t \Phi\right) dV = \int \Big(-\frac{v_E^2}{2R}\left[u^*, \hat{\rho}\right] - R\hat{\rho}\, w_E\left[u^*, \Phi\right] + R\left[u^*, P\right] \\ - u^*\nabla\phi\cdot\nabla\times\left(R^2\rho\left(\boldsymbol{v}_i^*\cdot\nabla\right)\boldsymbol{v}_E\right) - u^*\frac{1}{R}\left[\Psi, j\right] + u^*\frac{F_0}{R^2}\partial_\phi j + u^*\nabla\phi\cdot\nabla\times\left(R^2\mu\nabla^2\boldsymbol{v}_E\right)\Big) dV, \tag{13}$$

with u^* a test function, ϕ the toroidal direction, μ the dynamic viscosity and $\hat{\rho} = R^2\rho$. For

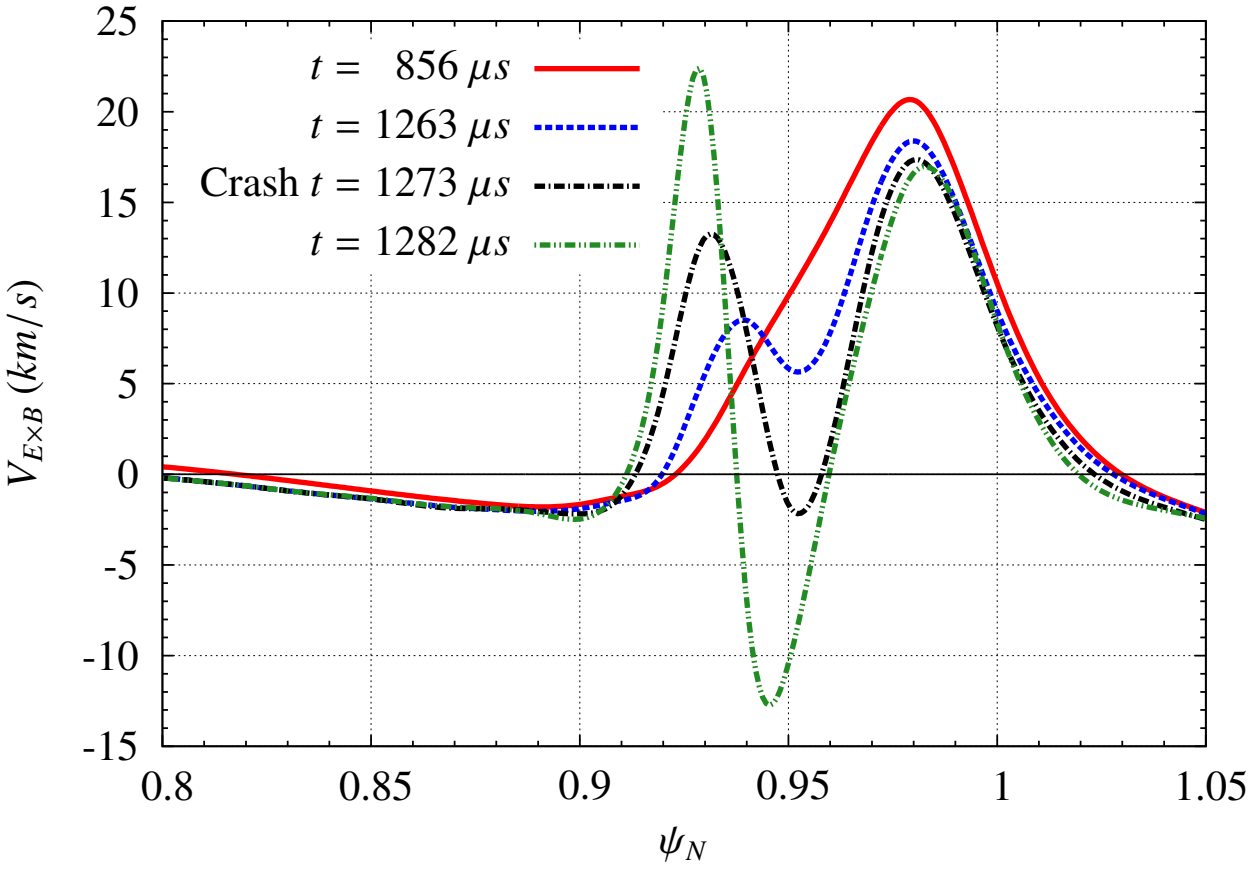


FIG. 6. Axisymmetric ($n = 0$) $\boldsymbol{E} \times \boldsymbol{B}$ velocity profiles during an ELM crash (averaged in the region between the low field side and the vertical direction $\theta = [0, \pi/2]$).

more details we refer to [12, 22, 23, 25].

In Fig. 7 the equilibrium noted Eq is the static equilibrium (pressure $R\,[u^*, P]$ plus Maxwell stress tensor, $R^{-1}\,[\Psi, j]$ term). Also axisymmetric equilibrium flows [27] generate viscous dissipation. We can observe that in the linear phase the static equilibrium Eq and viscosity terms balance, there is no vorticity generation. At $t = 1.24\ ms$, the diamagnetic term $-\nabla\phi{\cdot}\nabla\times(R^2\rho\,(\boldsymbol{v}_i^*\cdot\nabla)\,\boldsymbol{v}_E)$ (Dia) grows but is balanced by the equilibrium and viscosity terms. However a small growth of vorticity w_E is observed. Then at $t = 1.273\ ms$ (same time as in Fig. 5) the ELM crash occurs. The term $\delta_t w_E$ becomes large, strong vorticity is created. This vorticity is generated nonlinearly by the unbalance between the terms in the vorticity equation. The terms dominating the w_E dynamics are the Maxwell stress tensor $R^{-1}\,[\Psi, j]$ [12] (see also Fig. 5(c)) and the Dia term. On the other hand the pressure term $R\,[u^*, P]$ is large but does not behave with the same dynamic as the $\delta_t w_E$ term.

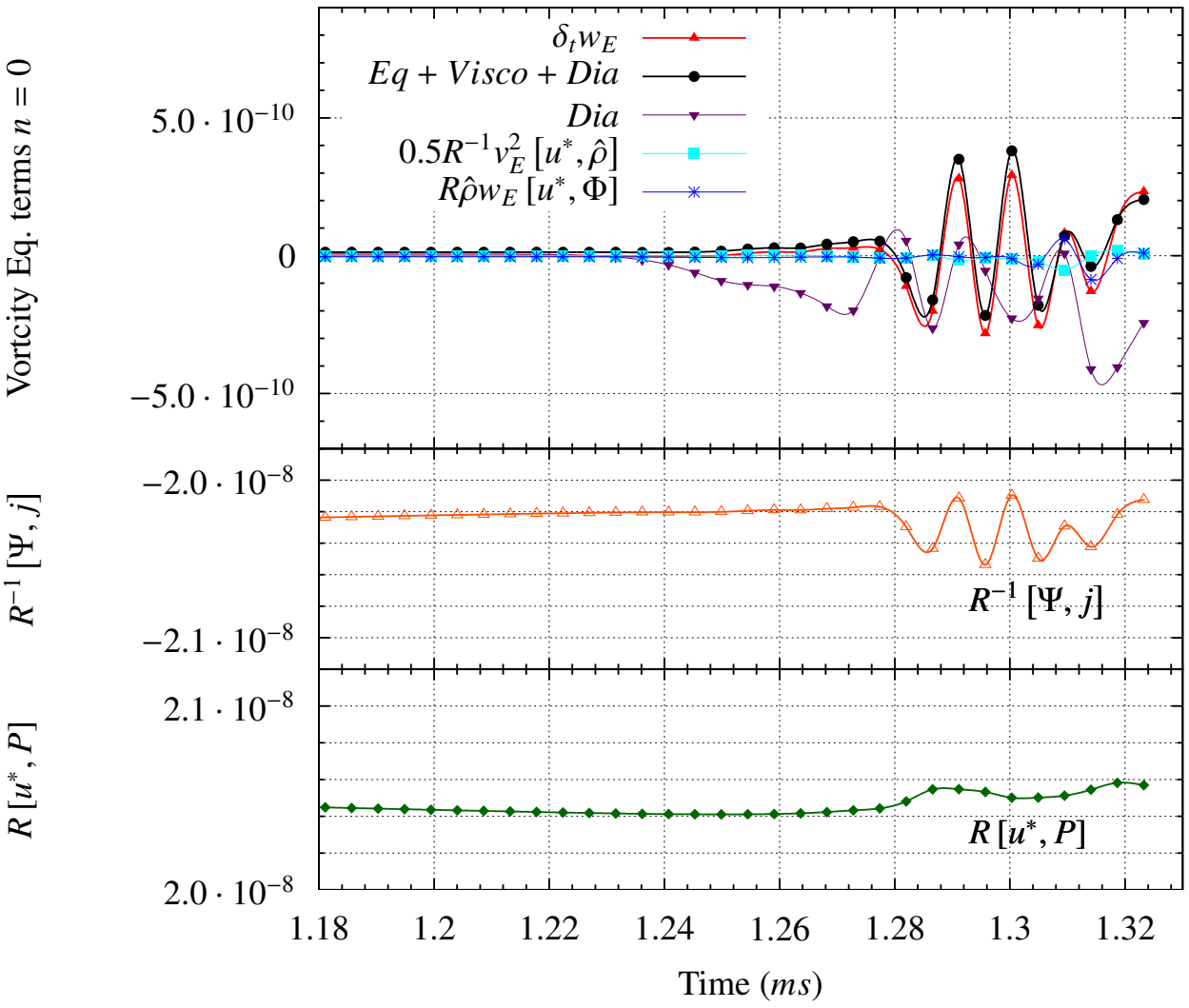


FIG. 7. Axisymmetric (toroidal mode number $n = 0$) $\boldsymbol{E}\times\boldsymbol{B}$ vorticity equation terms (see Eq. (13)) as a function of time.

IV. CONCLUSION

In the linear phase the analytical ideal ballooning calculations and the JOREK simulations are in good agreement. They explain why experimentally the ELM precursors are mainly observed rotating in the electron diamagnetic direction.

Near the ELM crash we find a strong nonlinear generation of axisymmetric $\boldsymbol{E}\times\boldsymbol{B}$ velocity shear. This shear makes the density filaments to be expelled outside the main plasma. Also the filaments rotation is opposite to the ELM precursors rotation, i.e., in the ion diamagnetic direction, as observed experimentally. The Maxwell stress and diamagnetic terms govern

the vorticity generation at the nonlinear phase.

The ELM crash is a strong nonlinear event (see e.g. [28]). In this letter we focus on the early stages of the ELM crash. We observe that the strong $\boldsymbol{E} \times \boldsymbol{B}$ shear plays an important role in the ELM filament detachment. Another important transport channel is parallel conduction [29]. Reconnection [30] is also observed at the early stages of the ELM crash and certainly plays an important role on the density and energy transport towards the plasma-facing components, in particular towards the tokamak divertor.

As a perspective for this work we can mention the study of the toroidal velocity profile. In this work we have not imposed a toroidal velocity source but it would certainly be an important element to take into account in future simulations of ELM precursors. The toroidal velocity profile not only influences the precursors rotation but also the linear ballooning dispersion relation if a shear exists (see e.g. [31]).

ACKNOWLEDGMENTS

We thank C. Norscini, P. Tamain and N. Fedorczak for interesting discussions on this work. This project has been carried out within the framework of the EUROfusion Consortium and has received funding from the Euratom research and training programme 2014-2018 under grant agreement No. 633053. This work has benefited from financial support from the National French Research Program (ANR): ANEMOS (2011). A part of this work was carried out using the CCRT-CURIE supercomputer within project GENCI (gen2197) and PRACE (ra1904) and the HELIOS supercomputer system (IFERC-CSC). The views and opinions expressed herein do not necessarily reflect those of the European Commission or the ITER Organization.

[1] A. Leonard, Physics of Plasmas **21**, 090501 (2014).

[2] G. Huijsmans, C. Chang, N. Ferraro, L. Sugiyama, F. Waelbroeck, X. Xu, A. Loarte, and S. Futatani, Physics of Plasmas **22**, 021805 (2015).

[3] G. Yun, W. Lee, M. Choi, J. Lee, H. Park, B. Tobias, C. Domier, N. Luhmann Jr, A. Donné, J. Lee, *et al.*, Physical Review Letters **107**, 045004 (2011).

[4] J. Boom, I. Classen, P. De Vries, T. Eich, E. Wolfrum, W. Suttrop, R. Wenninger, A. Donné,

B. Tobias, C. Domier, *et al.*, Nuclear Fusion **51**, 103039 (2011).

[5] I. Classen, J. Boom, A. Bogomolov, E. Wolfrum, M. Maraschek, W. Suttrop, P. de Vries, A. Donné, B. Tobias, C. Domier, *et al.*, Nuclear Fusion **53**, 073005 (2013).

[6] Y. Sechrest, T. Munsat, D. Battaglia, and S. Zweben, Nuclear Fusion **52**, 123009 (2012).

[7] R. Wenninger, H. Reimerdes, O. Sauter, and H. Zohm, Nuclear Fusion **53**, 113004 (2013).

[8] A. Kirk, D. Dunai, M. Dunne, G. Huijsmans, S. Pamela, M. Bécoulet, J. Harrison, J. Hillesheim, C. Roach, and S. Saarelma, Nuclear Fusion **54**, 114012 (2014).

[9] M. Rack, B. Sieglin, J. Pearson, T. Eich, Y. Liang, P. Denner, A. Wingen, L. Zeng, I. Balboa, S. Jachmich, *et al.*, Nuclear fusion **54**, 064012 (2014).

[10] P. Manz, J. Boom, E. Wolfrum, G. Birkenmeier, I. Classen, N. Luhmann Jr, U. Stroth, *et al.*, Plasma Physics and Controlled Fusion **56**, 035010 (2014).

[11] P. Snyder, H. Wilson, J. Ferron, L. Lao, A. Leonard, T. Osborne, A. Turnbull, D. Mossessian, M. Murakami, and X. Xu, Physics of Plasmas **9**, 2037 (2002).

[12] G. Huysmans and O. Czarny, Nuclear Fusion **47**, 659 (2007).

[13] O. Czarny and G. Huysmans, Journal of Computational Physics **227**, 7423 (2008).

[14] D. Schnack, D. Barnes, D. Brennan, C. Hegna, E. Held, C. Kim, S. Kruger, A. Pankin, and C. Sovinec, Physics of Plasmas **13**, 058103 (2006).

[15] J. Connor, R. Hastie, and J. Taylor, in *Proceedings of the Royal Society of London A: Mathematical, Physical and Engineering Sciences*, Vol. 365 (The Royal Society, 1979) pp. 1–17.

[16] P. Diamond, P. Similon, T. Hender, and B. Carreras, Physics of Fluids **28**, 1116 (1985).

[17] K. Roberts and J. Taylor, Physical Review Letters **8**, 197 (1962).

[18] W. Tang, R. L. Dewar, and J. Manickam, Nuclear Fusion **22**, 1079 (1982).

[19] G. Huysmans, S. Sharapov, A. Mikhailovskii, and W. Kerner, Physics of Plasmas **8**, 4292 (2001).

[20] G. Huysmans, Plasma Physics and Controlled Fusion **47**, B165 (2005).

[21] E. Viezzer, T. Pütterich, G. Conway, R. Dux, T. Happel, J. Fuchs, R. McDermott, F. Ryter, B. Sieglin, W. Suttrop, *et al.*, Nuclear Fusion **53**, 053005 (2013).

[22] S. Pamela, G. Huysmans, M. Beurskens, S. Devaux, T. Eich, S. Benkadda, *et al.*, Plasma Physics and Controlled Fusion **53**, 054014 (2011).

[23] F. Orain, M. Bécoulet, G. Dif-Pradalier, G. Huijsmans, S. Pamela, E. Nardon, C. Passeron, G. Latu, V. Grandgirard, A. Fil, *et al.*, Physics of Plasmas **20**, 102510 (2013).

[24] M. Bécoulet, F. Orain, G. Huijsmans, S. Pamela, P. Cahyna, M. Hoelzl, X. Garbet, E. Franck, E. Sonnendrücker, G. Dif-Pradalier, *et al.*, Physical Review Letters **113**, 115001 (2014).

[25] A. Fil, E. Nardon, M. Hoelzl, G. T. A. Huijsmans, F. Orain, M. Becoulet, P. Beyer, G. Dif-Pradalier, R. Guirlet, H. R. Koslowski, M. Lehnen, J. Morales, S. Pamela, C. Passeron, C. Reux, F. Saint-Laurent, and J. Contributors, Physics of Plasmas **22** (2015).

[26] N. Fedorczak, P. Diamond, G. Tynan, and P. Manz, Nuclear Fusion **52**, 103013 (2012).

[27] S. Pamela, G. Huysmans, and S. Benkadda, Plasma Physics and Controlled Fusion **52**, 075006 (2010).

[28] H. Wilson and S. Cowley, Physical Review Letters **92**, 175006 (2004).

[29] T. Rhee, S. S. Kim, H. Jhang, G. Y. Park, and R. Singh, Nuclear Fusion **55**, 032004 (2015).

[30] R. Fitzpatrick, Physics of Plasmas **1**, 3308 (1994).

[31] H. Wilson, P. Buxton, and J. Connor, *Rotation and momentum transport in magnetized plasmas (reviews of the theory of magnetized plasmas)*, edited by P. Diamond, X. Garbet, P. Ghendrih, and Y. Sarazin (World Scientific Publishing Co, 2015) Chap. 5.